A NETWORK FEM FOR COMPOSITE MATERIALS WITH A POSTERIOR ERROR CONTROL

M. EIGEL, D. PETERSEIM

ABSTRACT. A novel Finite Element Method (FEM) for the computational simulation in particle reinforced composite materials with many inclusions is presented. It is based on an adapted mesh which consists of triangles and parametric quadrilaterals in 2D. The number of elements and, hence, the number of degrees of freedom are proportional to the number of inclusions. The error of the method is independent of the distance of the neighboring inclusions. While being related to network methods, the approach can tackle more general settings. We present an efficient residual a posteriori error estimator which enables to compute reliable upper and lower error bounds. Several numerical examples illustrate the performance of the method and the error estimator. Moreover, it is demonstrated that the assumption of a lattice structure of inclusions can easily lead to incorrect predictions about material properties.

1. INTRODUCTION

Particle reinforced composite materials are engineered materials which consist of different constituents with the aim to obtain physical properties better than what the used materials have on their own. The specific properties of the composite material strongly depend on macroscopic parameters such as the volume fraction and microscopic geometric features of the constituents. They thus represent a typical multiscale problem for analysis and computation.

For this paper, the effective conductivity of two-phase materials consisting of many randomly dispersed highly conducting filler particles (inclusions) and a poorly conducting binder material (matrix) shall be investigated. Typically, the matrix material exhibits favourable mechanical features while the inclusions determine the "functional" properties. For our purposes, the contrast of conductivity between inclusions and matrix is high, i.e., in our model we assume the inclusions to be ideal conductors.

Date: September 25, 2012.

Key words and phrases. A posteriori, error analysis, finite element method, composite material, multiscale, high contrast, generalized Delaunay, network.

Although there are many results about how to analyse problems of this kind if the microstructure of the material is structured or periodic (homogenization theory), see e.g. [Kel63, KS64] and [ABP78, JKO94, CD00, BP89], the mathematical treatment is much less clear for unstructured distributions of particles. In particular, phenomena specific to the lack of a regular structure play a crucial role since they can be responsible for drastic changes in material properties when the composition of the material is changed only slightly. One such well-known phenomenon is the percolation effect [Kes92, Gri92] which can be observed for densely packed filler particles which occasionally form connected paths and thus strongly amplify the conducting property, see [BK01, BN02].

Since the prediction of the behaviour of a composite material on the one hand is crucial during the engineering process but on the other hand often is intractable analytically, numerical simulations can provide valuable insights with regard to effective material properties. Additionally, they can provide convenient means to test many different setups in order to obtain a specific material behaviour.

For the Poisson-type model problem with discontinuous diffusion coefficient (introduced in the next section), a classical numerical method is the finite element method (FEM) which is based on a partition of the domain. Due to the multiscale structure of the problem, in order to achieve accurate numerical results, the employed mesh would have to resolve the microstructure of the problem. Since inclusions are irregularly distributed in the matrix and their volume fraction is large, they often are close to touching one another. The material responses depend crucially on these tiny distances. Thus, they have to be resolved accurately by the underlying mesh. The generation of a mesh appropriate for numerical simulation for such a domain is difficult and requires the use of many elements which consequently leads to a (possibly prohibitively) high complexity in the solution process, see Figure 1 for a simple setting which already requires a very large number of mesh elements. As can be observed, the smallest FEM elements in Figure 1 scale like the minimal distance between inclusions.

Moreover, since the distribution of particles may be based on a random distribution, in order to determine the characteristic properties of a certain setup, a large set of realisations of the geometry has to be evaluated for the calculation of expected properties. Thus, the complexity for the required mesh generation and the resulting (linear) algebraic system to be solved are crucial and limiting factors.

The method promoted in this article is capable to yield accurate and reliable results for the described problem with low computational complexity. This is achieved by a specific partition of the domain which is inspired by discrete network methods [BP98, BK01, BN02] and resolves the inclusions

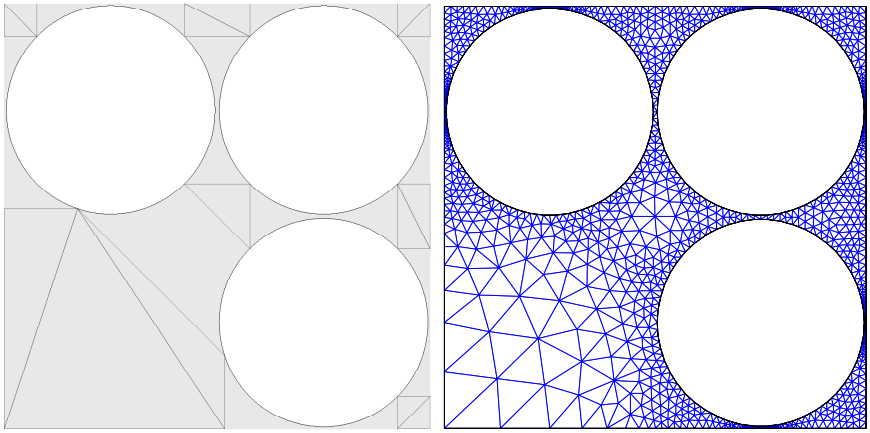

(a) Adapted mesh of Network FEM resolving 3 inclusions.

(b) FEM mesh resolving 3 inclusions.

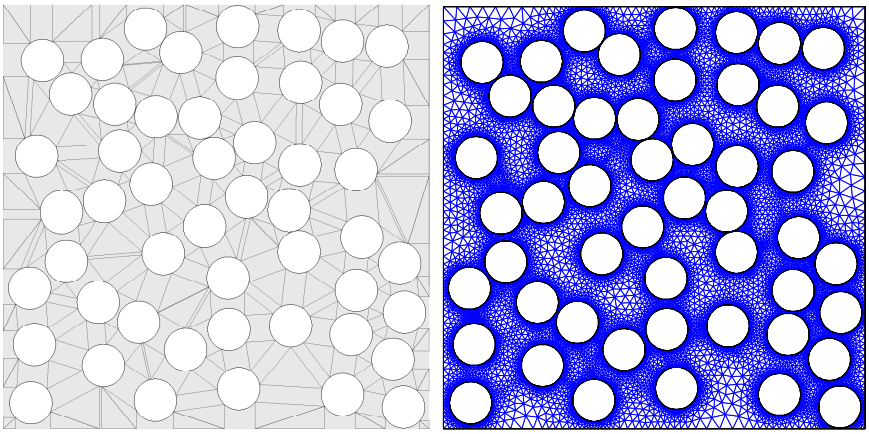

(c) Adapted mesh of Network FEM resolving 50 inclusions.

(d) FEM mesh resolving 50 inclusions.

FIGURE 1. Illustration of the mesh complexity for FEM and Network FEM based on two simple settings with 3 and 50 inclusions.

exactly while still remaining close to the classical FEM, both in implementation and the analytical results. Figure 1 also shows the adapted mesh which is of nearly optimal complexity, i.e. it the number of elements is proportional to the number of inclusions. In particular, the complexity does not scale with the infinitesimal distance between inclusions. Still, the discrete model accounts for the complexity of the microstructure and provides a good overall macroscopic response, see Sections 2 and 3.

1.1. **Model Problem.** We consider the Poisson model problem on some perforated domain $\Omega \subset \mathbb{R}^2$ which results from some simply connected polygonal domain $\Omega^* \subset \mathbb{R}^2$ by removing a union of circular inclusions Ω_{inc}.

The set of closed, pairwise disjoint discs with positive radii is denoted $\mathcal{B}_{\mathrm{inc}} \subset \Omega$, i.e., for any $B_1, B_2 \in \mathcal{B}_{\mathrm{inc}}$ with $B_1 \neq B_2$,

$$B_1, B_2 \subset \Omega \quad \text{and} \quad \operatorname{dist}(B_1, B_2) > 0. \tag{1.1}$$

The two phases of the material are represented by the set of the inclusions Ω_{inc} and the so-called matrix Ω,

$$\Omega_{\mathrm{inc}} := \bigcup_{B \in \mathcal{B}_{\mathrm{inc}}} \operatorname{int}(B) \quad \text{and} \quad \Omega := \Omega^* \setminus \Omega_{\mathrm{inc}}. \tag{1.2}$$

We assume the number of inclusions $N_{\mathrm{inc}} := \#\mathcal{B}_{\mathrm{inc}}$ to be very large such that Ω_{inc} occupies a significant amount of the volume of Ω^*.

The problem then reads

$$-\operatorname{div} \nabla u = f \quad \text{in } \Omega, \tag{1.3a}$$

$$u = u_D \quad \text{on } \Gamma_D, \tag{1.3b}$$

$$\partial_n u \cdot n_\Omega = 0 \quad \text{on } \Gamma_N, \tag{1.3c}$$

$$\forall B \in \mathcal{B}_{\mathrm{inc}}: \quad u|_{\partial B} \equiv \text{const} \quad \text{and} \quad \int_{\partial B} \frac{\partial u}{\partial n_B}\, ds = 0, \tag{1.3d}$$

with $f \in L^2(\Omega)$, also see [BK01]. The outer normal to some Lipschitz domain ω is denoted by n_ω. Sufficiently smooth Dirichlet boundary data u_D is imposed on the closed set $\Gamma_D \subset \partial\Omega^*$ with positive surface measure while homogeneous Neumann data is prescribed on $\Gamma_N := \partial\Omega^* \setminus \Gamma_N$. To reduce technical overhead, we will assume later that u_D is included in our discrete space, i.e., u_D is piecewise affine with respect to some subdivision of Γ_D. Otherwise, errors due to the approximation of the boundary values have to be considered.

Define the vector space

$$V := \left\{ v \in H^1(\Omega) \mid v_{\Gamma_D} = 0 \text{ and } \forall B \in \mathcal{B}_{\mathrm{inc}}\ \exists\, c_B \in \mathbb{R} : v|_{\partial B} = c_B \right\}.$$

The weak solution u of formulation (1.3) is equivalent to the minimisation of the quadratic energy functional

$$\mathcal{E}(v) := \frac{1}{2} \int_\Omega |\nabla v(x)|^2\, dx - \int_\Omega f(x) v(x)\, dx \quad \text{amongst all } v \in u_D + V. \tag{1.4}$$

The variational form of (1.3) reads: Find $u \in u_D + V$ such that, for all $v \in V$,

$$a(u, v) := \int_\Omega \nabla u \cdot \nabla v\, dx = \int_\Omega f v\, dx =: F(v). \tag{1.5}$$

Recall that $\nabla u|_{\Omega^* \setminus \Omega} = 0$. Then, for $v \in V$, the coercivity of the continuous bilinear form a can readily be seen by

$$a(v,v) = \int_{\Omega} |\nabla v|^2 \, dx = \int_{\Omega^*} |\nabla v|^2 \, dx \gtrsim \|v\|^2_{H^1(\Omega^*)} \gtrsim \|v\|_{H^1(\Omega)} . \tag{1.6}$$

With this, the symmetry and boundedness of a, and the boundedness of F, Equation (1.5) exhibits a unique solution.

1.2. **Outline.** Section 2 presents the novel Network FEM (NFEM) [CP12]. We describe the underlying subdivision which exactly represents the geometry of the domain. The globally continuous approximation space is build as the union of local transformations of affine spaces on parametrized quadrilaterals and triangles. The crucial point is that the dimension of the resulting space is the same as the number of inclusions due to the construction of the adapted triangulation. Thus, the complexity of the discretization is proportional to the complexity of the geometry representation (centers and radii of inclusions) and, hence, (quasi-)minimal. Interpolation error estimates and a priori error bounds are recalled. Section 3 is concerned with the derivation of some residual a posteriori error estimator which provides a computable error bound of the error of the discrete solution. It potentially also could steer an adaptive algorithm. We prove reliability and efficiency of the error estimator which, while being based on well-known arguments from classical FEM, requires some new non-trivial estimates due to the specific features of the adapted mesh. Numerical validation of the Network FEM and the a posteriori error estimator is given in Section 4. The percolation phenomenon is shown experimentally. It can be observed when the inclusions reach a very high density such that they are in contact with neighboring inclusions. A remarkable observation is that the common modelling assumption of a structured distribution leads to fundamentally different results than random distributions of inclusions even when the volume fraction is identical. We finish in Section 5 with some conclusions and an outlook.

1.3. **Notation.** We use the common notation for Sobolev spaces of functions defined on a domain $\Omega \subset \mathbb{R}^2$. By $H^k(\Omega)$ the space of all functions in $L^2(\Omega)$ which exhibit weak derivatives up to order k is defined.

2. Network FEM

In this section, we recall the problem-adapted mesh and the construction of the conforming piecewise affine discrete approximation space [CP12]. The mesh has to take into account the geometrical features of the domain, i.e. many circular inclusions, which is achieved by a combination of curvilinear quadrilaterals and triangle elements.

2.1. **Grid Construction.** The geometry of the problem is determined by the set of (finitely many) closed discs $\mathcal{B}$. Each $B \in \mathcal{B}$ is defined by its center $c_B = \mathrm{mid}(B)$ and the radius $r_B := \mathrm{diam}(B)/2 \geq 0$. Note that also discs with radius zero are admissible. The elements of $\mathcal{B}$ are denoted as *generalized vertices*. They are partitioned into the set of inclusions $\mathcal{B}_{\mathrm{inc}}$ and discs with vanishing radius $\mathcal{B}_{\mathrm{mat}}$

$$\mathcal{B} = \mathcal{B}_{\mathrm{inc}} \cup \mathcal{B}_{\mathrm{mat}} \quad \text{and} \quad \mathcal{B}_{\mathrm{inc}} \cap \mathcal{B}_{\mathrm{mat}} = \emptyset.$$

The set $\mathcal{B}_{\mathrm{mat}}$ contains the corner points of the domain and all points where the boundary condition switches from Neumann to Dirichlet. Additionally, in order to control the approximation quality, other points can be added to the set $\mathcal{B}_{\mathrm{mat}}$. This for instance can be done by an adaptive algorithm based on the residual error estimator described in Section 3.

The algorithm for the construction of the adapted mesh is summarized in an algorithmic fashion in the appendix.

For the transformation from a reference rectangle to parametric quadrilaterals (and triangles), we apply the following mapping.

Definition 2.1 (mapping onto parametric quadrilaterals)**.** Consider the circular inclusions $B_1, B_2 \in \mathcal{B}$, $B_1 \cap B_2 = \emptyset$, with radii r_1, r_2 and connecting quadrilateral $T \in \mathcal{T}^Q$. The coordinate system can be rotated such that, without loss of generality, the centers of the discs are given by $c_1 = (0,0)$ and $c_2 = (0,\delta)$ and $\delta > r_1 + r_2$. With angles $-\pi/2 \leq \alpha \leq \beta \leq \pi/2$, define the map $J_T :]\alpha,\beta[\times]0,1[\to \mathrm{int}(E)$ by

(2.1)
$$J_T(s,\lambda) := \left((1-\lambda)r_1 + \lambda r_2 \frac{r_1 + H(s)}{r_2 + H(s)}\right)\begin{bmatrix}\sin(s)\\ \cos(s)\end{bmatrix} + \delta\lambda\left(1 - \frac{r_2}{r_2 + H(s)}\right)\begin{bmatrix}0\\1\end{bmatrix},$$

where

$$H(s) := \frac{\left(\delta^2 - 2\,\cos(s)\,\delta\, r_1\right) + r_1^2 - r_2^2}{(2\,r_2 - 2\,r_1) + 2\,\delta\,\cos(s)}.$$

See Figure 3a in [CP12] for an illustration.

2.1.1. *Local mesh size.* For any triangle $T \in \mathcal{T}^T$, $h_T := \mathrm{diam}(T)$ denotes its size. Analogously, for any edge $E \in \mathcal{E}$, i.e. $h_E = \mathrm{diam}(E)$. For $T \in \mathcal{T}^Q$, the definition of the mesh size h_T is more involved since it is subject to the mapping J_T of Definition 2.1. We set, for $x \in T$ and $(s,\lambda) = J_T^{-1}(x)$,

$$h(x) := \|J_T(s,1) - J_T(s,0)\|_{\mathbb{R}^2}.$$

Note that h varies within each quadrilateral. Then, the global mesh size function h is defined by

$$h|_T := h_T \qquad \text{for } T \in \mathcal{T}.$$

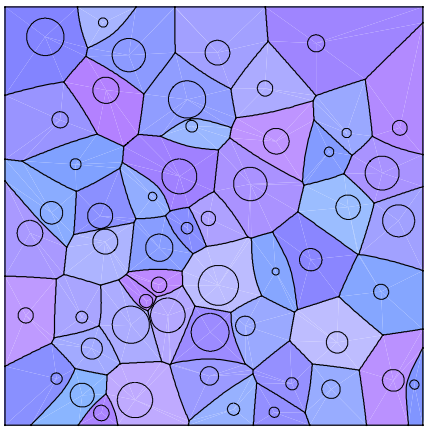

(a) Generalized Voronoi cells for set $\mathcal{B}$ of discs.

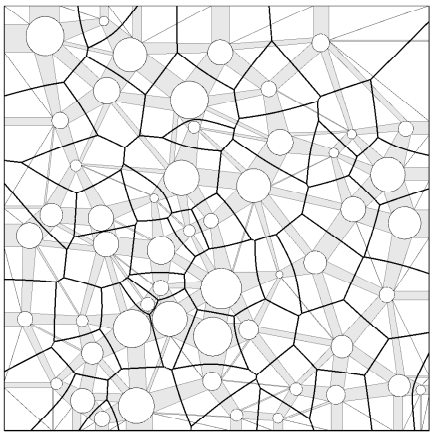

(b) Parametric quadrilaterals $\mathcal{T}^Q$ (shaded in gray) connecting any two discs of $\mathcal{B}$ which are associated to some Voronoi edge in $\mathcal{E}_\circ$ (black curves).

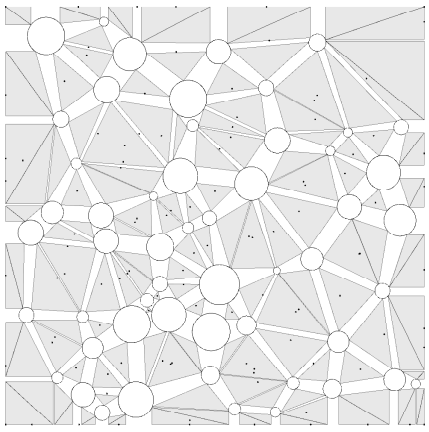

(c) Triangles $\mathcal{T}^T$ (shaded in gray) associated to Voronoi vertices (black dots) occupy the remaining space between quadrilaterals of $\mathcal{T}^Q$.

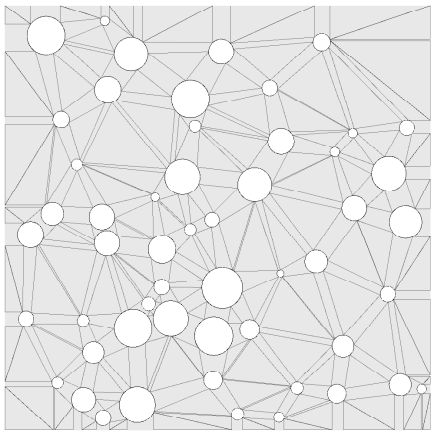

(d) Final grid $\mathcal{T} = \mathcal{T}^Q \cup \mathcal{T}^T$ (shaded in gray) consisting of parametric quadrilateral and triangular elements.

FIGURE 2. Illustration of the grid construction in Section 2.1.

Moreover, we define the vertex and edge patches

$$\text{for } B \in \mathcal{B}: \quad \omega_B := B \cup \{T \in \mathcal{T} : \ T \cap B \neq \emptyset\},$$
$$\text{for } E \in \mathcal{E}: \quad \omega_E := B \cup \{T \in \mathcal{T} : \ T \cap E \neq \emptyset\}.$$

2.2. **Finite Element Space.** The discrete approximation space has the same dimension as the cardinality of the set of vertices $|\mathcal{B}|$ of the triangulation as in standard first-order FEM. Dirichlet boundary nodes are fixed and thus do

not contribute to the complexity of the linear system. Every $B \in \mathcal{B}$ defines a local affine basis function $\lambda_B : \mathbb{R}^2 \to [0,1]$ with

$$\lambda_B \equiv 1 \text{ on } B \quad \text{and} \quad \lambda_B \equiv 0 \text{ on } \mathcal{B} \setminus B.$$

The support of λ_B is given by

$$\operatorname{supp}(\lambda_B) = B \cup \omega_B$$

The transformation of affine base functions onto parametric quadrilaterals (and triangles) can be achieved by the mapping of Definition 2.1. Figure 3 depicts the map and a transformed base function associated to some disc.

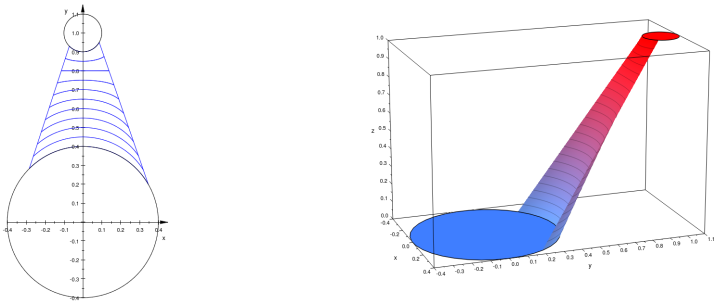

FIGURE 3. Map to parametric quadrilateral (isolines) [left] and transformed affine base function [right].

Note that the set of basis functions $\Lambda := \{\lambda_B : B \in \mathcal{B}\}$ forms a partition of unity in Ω. The finite element space

$$S := \operatorname{span}(\Lambda) \cap V$$

is then spanned by the nodal basis functions λ_B of all $B \in \mathcal{B}$ which do not correspond to nodes on the Dirichlet boundary Γ_D.

The discrete problem reads: Find $u_{\mathrm{NFEM}} \in u_D + V$ such that, for all $v \in V$,

$$a(u_{\mathrm{NFEM}}, v) = F(v).$$

The error of the discrete solution $u_{\mathrm{NFEM}} \in u_D + V$ satisfies [CP12]

$$\|\nabla(u - u_{\mathrm{NFEM}})\|_{L^2(\Omega)} \lesssim \left\|h\nabla^2 u\right\|_{L^2(\Omega)}. \tag{2.2}$$

Moreover, the solution u satisfies [Pet12]

$$\left\|h\nabla^2 u\right\|_{L^2(\Omega)} \lesssim \|f\|_{L^2(\Omega)}. \tag{2.3}$$

Note that the implicit constants in the previous two estimates do not depend on the tiny distances between neighboring inclusions.

3. A Posteriori Estimator

A posteriori error control allows to assess the quality of the discrete solution and provides upper and lower bounds for the global error. Although it is well established with standard FEM, see [AO00, Ver96], an extension to NFEM is not immediate. Instead, it requires the application of some non-trivial interpolation estimates as detailed in Subsection 3.1.

This section is concerned with the derivation of some residual a posteriori error estimator η based on a mesh $\mathcal{T}$. The aim of the estimator is to bound the error $e := u - u_{\mathrm{NFEM}}$ in the energy norm. Two-sided bounds ensure that the estimator is sufficiently accurate.

Define the interior and the edge residual r_T and r_E by

$$r_T := f + \operatorname{div}_{\mathcal{T}} \nabla_{\mathcal{T}} u_{\mathrm{NFEM}} \quad \text{in } T \in \mathcal{T},$$

$$r_E := \begin{cases} -\nabla u_{\mathrm{NFEM}} \cdot n_E & \text{on } \mathcal{E}(\Gamma_N), \\ -[\nabla u_{\mathrm{NFEM}} \cdot n_E]_E & \text{on all other } E \in \mathcal{E} \end{cases}$$

and set $\tilde{r}_T := r_T + (f_T - f)$. By the subscript in $\operatorname{div}_{\mathcal{T}}$ and $\nabla_{\mathcal{T}}$ we denote the piecewise application of the differential operator.

The error estimator then reads

$$\eta := \left(\sum_{T \in \mathcal{T}} \|h_T r_T\|^2_{L^2(T)} + h_E \|r_E\|^2_{L^2(\partial T)} \right)^{1/2}$$

where r_T and r_E are some computable functions of u_{NFEM}. We call an estimator reliable if $\|\nabla e\|_{L^2(\Omega)} \lesssim \eta$ and efficient if $\eta \lesssim \|\nabla e\|_{L^2(\Omega)}$.

In estimates, the notation $A \lesssim B$ abbreviates $A \leq CB$ with some multiplicative constant $C > 0$ which only depends on the domain Ω and the shape but not on the mesh size h of finite element domains. Furthermore, $A \approx B$ abbreviates $A \lesssim B \lesssim A$.

The main result is the following theorem.

Theorem 3.1. *Given the discrete solution $u_{NFEM} \in u_D + V$, the a posteriori error estimator η is reliable and efficient, i.e., with oscillations* (3.1)*, it holds*

$$\|\nabla(u - u_{NFEM})\|_{L^2(\Omega)} \lesssim \eta \qquad \text{and}$$
$$\eta \lesssim \|\nabla(u - u_{NFEM})\|_{L^2(\Omega)} + \operatorname{osc}(f, \mathcal{T}).$$

Remark 3.1. The first estimate is independent of all mesh related parameters except the angles of the elements. The implicit constants in the second estimate depend on the possible anisotropy of elements $T \in \mathcal{T}^Q$, i.e., on the ratio $\operatorname{diam}(T)/\sqrt{|T|}$. Since we are mainly interested in numerical experiments where the reliability of the estimator is crucial, we do not further investigate this issue.

The proof is provided in Subsections 3.2 and 3.3. The specific properties of the adapted mesh and the respective discrete space impose complications in the derivation which are not encountered in standard FEM. This is reflected by the fact that the mesh size h_T enters some norms since it is non-constant on the elements $\mathcal{T}^Q \subset \mathcal{T}$.

Higher-order terms due to properties of the data enter the estimates in the form of oscillations. On some $T \in \mathcal{T}$, let $f_T := |T|^{-1} \int_T f \, dx$ be the piecewise constant average of $f \in L^2(\Omega)$. The global piecewise constant function $f_{\mathcal{T}}$ is defined by $f_{\mathcal{T}}|_T = f_T$ for $T \in \mathcal{T}$. Then, define oscillations on $\mathcal{T}$ by

$$\operatorname{osc}(f, \mathcal{T}) := \|h_{\mathcal{T}}(f - f_{\mathcal{T}})\|_{L^2(\Omega)} . \tag{3.1}$$

In the following, we prove the reliability of the a posteriori estimator independent of the geometry of Ω.

3.1. **Quasi-Interpolation.** We will use the quasi-interpolation operator $I : V \to S$ defined for $v \in V$ by

$$\begin{aligned} Iv|_{\partial B} &= v|_{\partial B} \quad \text{for } B \in \mathcal{B}_{\text{inc}} \quad \text{and} \\ (Iv)(B) &= |\omega_B|^{-1} \int_{\omega_B} v \, dx \quad \text{for } B \in \mathcal{B}_{\text{mat}}. \end{aligned} \tag{3.2}$$

Lemma 3.2. Let $u \in V$. Then the following estimates hold with constants independent of the (local) mesh size h and the diameter of the discs in $\mathcal{B}$.

For all $T \in \mathcal{T}$,

$$\left\| h_T^{-1}(u - Iu) \right\|_{L^2(T)} \lesssim \|u\|_{H^1(T)} . \tag{3.3}$$

For all $E \in \mathcal{E}$,

$$\|u - Iu\|_{L^2(E)} \lesssim h_E^{1/2} \|u\|_{H^1(\omega_E)} . \tag{3.4}$$

We emphasise that, depending on the type of element $T \in \mathcal{T}$, the mesh size h_T does not have to be constant.

Proof. We first prove (3.4). Let $E \in \mathcal{E}$ and let $T \in \mathcal{T}^T$ be some triangle with edge E. According to [CF00], the trace inequality for H^1 functions yields

$$\|u - Iu\|_{L^2(E)} \lesssim h_E^{1/2} \|\nabla(u - Iu)\|_{L^2(\mathcal{T})} + h_E^{-1/2} \|u - Iu\|_{L^2(T)} . \tag{3.5}$$

The stability and approximation properties of the (Clément) interpolation operator yield

$$h_T^{-1} \|u - Iu\|_{L^2(T)} \lesssim \|\nabla u\|_{L^2(\omega_T)} \tag{3.6}$$

with the element patch $\omega_T := \cup\{T' \in \mathcal{T} : \overline{T} \cap \overline{T'} \neq \emptyset\}$. The combination of (3.5) and (3.6) is (3.4).

The proof of (3.3) for $T \in \mathcal{T}^T$ follows from (3.6). To prove (3.3) with $T \in \mathcal{T}^Q$, we employ a similar construction as in the proof of Lemma 3.3 in [CP12]. Without loss of generality, let $T \in \mathcal{T}^Q$ be connected, $r_{B_1} \geq r_{B_2}$, and $c_{B_1} = 0$, $c_{B_2} = (0, \delta)$ for some $\delta > r_{B_1} + r_{B_2}$. The restriction $T \cap \partial B_1 = \phi([\alpha, \beta])$ of T to B_1 shall be parametrized by some angle $s \in [\alpha, \beta] \subset [-\pi/2, \pi/2]$ with $\phi(s) := r_{B_1}(\sin(s), \cos(s))$. The parameter interval $[\alpha, \beta]$ is subdivided by equidistributed points

$$\alpha = s^1 < s^2 < s^3 < \ldots < s^L = \beta.$$

These points are mapped (cf. Definition 2.1) by $J(\cdot, 0)$ onto B_1 and by $J(\cdot, 1)$ onto B_2. Let

$$\begin{aligned} Q_L(T) &:= \{Q_\ell \ : \ell = 1, \ldots, L-1\} \quad \text{with} \\ Q_\ell &:= \operatorname{conv}\{J(s^\ell, 0), J(s^{\ell+1}, 0), J(s^\ell, 1), J(s^{\ell+1}, 1)\} \end{aligned}$$

be a subdivision of T into quadrilaterals, see Figure 4.

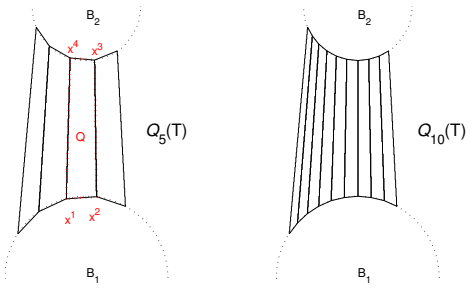

FIGURE 4. Subdivisions $Q_5(T)$ and $Q_{10}(T)$ of some parametric quadrilateral $T = \mathcal{E}_\circ(B_1, B_2) \in \mathcal{T}^Q$ into 5 and 10 quadrilaterals in the proof of Lemma 3.2.

The union of quadrilaterals on level L provides a polygonal approximation $T^L := \bigcup_{Q \in Q_L(T)} Q$ of T with $T \subset T^L \subset \operatorname{conv} T$ for all L and $|T^L \setminus T| \to 0$ as $L \to \infty$. Let u_T denote some bounded extension of $u|_T$ to $\mathbb{R}^2$ in the sense of [Ste70].

The nodal (bilinear) interpolation operator with respect to $Q \in Q_L$ is denoted by I_Q and its Q_L-piecewise version by I_{Q_L}. Theorem 3.8 from [MNS09] implies

$$\operatorname{diam}(Q)^{-1} \left\| u_T - I_Q u_T \right\|_{L^2(Q)} \leq C_Q \, \|\nabla u_T\|_{L^2(Q)} \tag{3.7}$$

for all $Q \in \mathcal{Q}_L$ and $L \in \mathbb{N}$. The constant C_Q depends only on the interior angles of Q, i.e., C_Q can be bounded uniformly for all $Q \in \mathcal{Q}_L$ and all $L \in \mathbb{N}$. Thus,

$$\begin{aligned} \|h_T^{-1}(u_T - I_{\mathcal{Q}_L} u_T)\|^2_{L^2(T^L)} &\lesssim \sum_{Q\in\mathcal{Q}_L} \|u_T - I_Q u_T\|^2_{L^2(Q)} \left\|h_T^{-1}\right\|^2_{L^\infty(Q)} \\ &\overset{(3.7)}{\lesssim} \sum_{Q\in\mathcal{Q}_L} \|\nabla u_T\|^2_{L^2(Q)}. \end{aligned} \tag{3.8}$$

The implicit constants in this estimate only depend on the interior angles of Q. Let L tend to infinity in (3.8) to verify

$$\|h_T^{-1}(u - \tilde{u})\|^2_{L^2(T)} \lesssim \|\nabla u\|^2_{L^2(T)} \tag{3.9}$$

with $\tilde{u} := \lim_{L\to\infty} I_{\mathcal{Q}_L} u_T$. Since $Iu = \tilde{u}$, the proof is finished. □

3.2. **Proof of Reliability.** We define the residual $\mathcal{R}es \in V^*$ for all $v \in V$ by

$$\mathcal{R}es(v) := a(e, v) = F(v) - a(u_{\mathrm{NFEM}}, v). \tag{3.10}$$

Note that the test space of the Galerkin method V employed to obtain u_{NFEM} is in the kernel of the residual. Together with some interpolation estimates, the Galerkin orthogonality $S \subset \ker \mathcal{R}es$ is key in the derivation of residual estimators.

Since $Iv \in S$ is an admissible test function for any $v \in V$, Galerkin orthogonality and element-wise integration by parts yield

$$a(e, v) = a(e, v - Iv).$$

We write the integrals of (3.10) as sum over the elements of $\mathcal{T}$ which gives, for $v \in V$,

$$a(e, v - Iv) = \sum_{T\in\mathcal{T}} \left\{ \int_T f(v - Iv)\, dx - \int_T \nabla u_{\mathrm{NFEM}} \cdot \nabla(v - Iv)\, dx \right\}$$

Recall that $(v - Iv)|_{\cup\mathcal{B}_{\mathrm{inc}}} = 0$ from (3.2). Then, integration by parts and rearranging terms yields

$$a(e, v - Iv) = \sum_{T\in\mathcal{T}} \int_T r_T(v - Iv)\, dx + \sum_{E\in\mathcal{E}_{\mathrm{int}}} \int_E r_E(v - Iv)\, ds.$$

By use of Cauchy-Schwarz,

$$a(e, v) \le \sum_{T\in\mathcal{T}} \|h_T r_T\|_{L^2(T)} \left\|h_T^{-1}(v - Iv)\right\|_{L^2(T)} + \sum_{E\in\mathcal{E}_{\mathrm{int}}} \|r_E\|_{L^2(E)} \|v - Iv\|_{L^2(E)}.$$

With the interpolation estimates of Lemma 3.2 and another application of Cauchy-Schwarz, we arrive at

$$a(e,v) \lesssim \|v\|_{H^1(\Omega)} \left\{ \sum_{T\in\mathcal{T}} \|h_T r_T\|^2_{L^2(T)} + \sum_{E\in\mathcal{E}_{\text{int}}} h_E \|r_E\|^2_{L^2(E)} \right\}^{1/2}.$$

With $v = e$ we obtain the error estimate

$$\|\nabla e\|^2_{L^2(\Omega)} \lesssim \sum_{T\in\mathcal{T}} \|h_T r_T\|^2_{L^2(T)} + \sum_{E\in\mathcal{E}_{\text{int}}} h_E \|r_E\|^2_{L^2(E)} = \eta^2.$$

3.3. **Proof of Efficiency.** The efficiency of η can be derived by a combination of standard arguments, see [Ver96], and the interpolation error estimates of Subsection 3.1.

We denote by $\psi_T \in H^1_0(T)$ the usual element bubble function on $T \in \mathcal{T}$ and by $\psi_E \in H^1_0(\omega_E)$ the usual edge bubble function with support on the patch ω_E of edge $E \in \mathcal{E}$, see [Ver96] for details. The definition of bubble functions on triangular and quadrilateral elements can also be found in [AO00]. Note that an edge bubble function ψ_E is continuous along $E \in \mathcal{E}$ in both configurations which may occur, i.e., for some $T_1, T_2 \in \mathcal{T}^T$ and $Q \in \mathcal{T}^Q$, $E = T_1 \cap T_2$ or $E = T_1 \cap Q$.

In any case, the usual estimates for edge bubbles hold, see e.g. [Ver96]. For $T \in \mathcal{T}^Q$, we set $\psi_T = \psi_{T_{\text{ref}}} \circ J_T^{-1}$ the pull-back onto the bubble function of the reference square. Local efficiency is first shown for the volume residual, then for the edge residual.

For some element $T \in \mathcal{T}$, we set $v_T := \psi_T \tilde{r}_T$ and deduce

$$\begin{aligned}
\|h_T \tilde{r}_T\|^2_{L^2(T)} &\lesssim \int_T h_T^2 \tilde{r}_T v_T \, dx \\
&= \mathcal{R}es(h_T^2 v_T) - \int_T (f - f_T) h_T^2 v_T \, dx \\
&\leq \|\nabla(u - u_{\text{NFEM}})\|_{L^2(T)} \left\|\nabla(h_T^2 v_T)\right\|_{L^2(T)} \\
&\qquad + \|h_T(f - f_T)\|_{L^2(T)} \|h_T v_T\|_{L^2(T)} \\
&\lesssim \left(\|\nabla e\|_{L^2(T)} + \|h_T(f - f_T)\|_{L^2(T)} \right) \\
&\qquad \times \|h_T \tilde{r}_T\|_{L^2(T)}.
\end{aligned}$$

Here, we have used the inverse inequality $\left\|\nabla(h_T^2 \tilde{r}_T)\right\|_{L^2(T)} \lesssim \|h_T \tilde{r}_T\|_{L^2(T)}$ on $T \in \mathcal{T}$ for any $v \in V(T)$ with a constant independent of the mesh size h_T and $h_T \nabla \psi_T \leq C$ with C depending on anisotropy $\text{diam}(T)/\sqrt{|T|}$. Such inverse estimates are standard for classical FEM and can be proved with techniques as in [Pet12]. With the split

$$\|h_T r_T\|_{L^2(T)} \leq \|h_T \tilde{r}_T\|_{L^2(T)} + \|h_T(f - f_T)\|_{L^2(T)}$$

we obtain

$$\|h_T r_T\|_{L^2(T)} \lesssim \|\nabla e\|_{L^2(T)} + \operatorname{osc}(f, T).$$

Note that along some edge $E \in \mathcal{E} \setminus \Gamma_D$ with $E = T_+ \cap T_-$, $T_+, \mathcal{T}_- \in \mathcal{T}$, the jump $[\nabla u_{\mathrm{NFEM}} \cdot n_E]_E$ is not constant. Let $v_E : \omega_E \to \mathbb{R}$ be the piecewise (with regard to T_+ and T_-) harmonic function with $v_E|_E = \psi_E [\nabla u_{\mathrm{NFEM}} \cdot n_E]_E$ and $v_E|_{\partial\omega_E} = 0$. We derive as before

$$\begin{aligned}
\|[\nabla u_{\mathrm{NFEM}} \cdot n_E]_E\|^2_{L^2(E)} &\lesssim \int_E [\nabla u_{\mathrm{NFEM}} \cdot n_E]_E v_E \, ds \\
&= \int_{\omega_E} r_T v_E \, dx - \mathcal{R}es(v_E) \\
&\lesssim \|r_T\|_{L^2(\omega_E)} \|v_E\|_{L^2(\omega_E)} + \|\nabla e\|_{L^2(\omega_E)} \|\nabla v_E\|_{L^2(\omega_E)} \\
&\lesssim \left(h_E^{1/2} \|r_T\|_{L^2(\omega_E)} + h_E^{-1/2} \|\nabla e\|_{L^2(\omega_E)} \right) \\
&\qquad \times \|[\nabla u_{\mathrm{NFEM}} \cdot n_E]_E\|_{L^2(E)} .
\end{aligned}$$

The constant in the trace inequality depends on anisotropy. This, (3.3) and a triangle inequality yields the assertion

$$\|[\nabla u_{\mathrm{NFEM}} \cdot n_E]_E\|_{L^2(E)} \lesssim h_E^{1/2} \|f + \operatorname{div}_{\mathcal{T}} \nabla u_{\mathrm{NFEM}}\|_{L^2(\omega_E)} + h_E^{-1/2} \|\nabla e\|_{L^2(\omega_E)} .$$

Note that edges on the Neumann boundary can be treated in the same way.

4. Numerical Examples

This section is concerned with the practical assessment of the Network FEM described in Section 2. In Subsection 4.1, the percolation effect is demonstrated with domains with many densely packed inclusions. When the density of filler particles becomes high enough, connected paths through the domain can emanate which leads to a strong increase of the energy of the solution. We demonstrate that the energy of the solution u_{NFEM} depends on the density of particles and on their distance. It is illustrated numerically that the error is basically independent of the inclusion distance and thus of the energy $\mathcal{E}(u_{\mathrm{NFEM}})$.

In Subsection 4.2 we compare the simulation of inclusions distributed in a structured and in a random way. The striking observation is that for identical volume fraction, i.e. the same number of inclusions, the two settings exhibit completely different properties. While percolation can be seen in the structured case, the energy $\mathcal{E}(u_{\mathrm{NFEM}})$ stays nearly constant with random particle distributions. Since many methods for multiscale problems like several popular multiscale FEM and classical homogenization assume periodicity of the microscale in the limit, this finding strongly supports the explicit resolution of the actual microscale structure as pursued in the presented Network FEM.

For all computations, model problem (1.3) on the square domain $\Omega^* := [0,1]^2$ with equi-sized inclusions is employed. On the left and right boundary, homogeneous Neumann boundary data is prescribed. Dirichlet data is set on the top and bottom boundaries with $u|_{y=0} = 0$ and $u|_{y=1} = 1$. Since the problem can be regarded as stochastic due to the randomly distributed particles, a set of realisations is computed and statistics are evaluated afterwards.

In order to obtain an adequate boundary representation with the grid, we mirror the perforated domain Ω along all four sides and also along the four corners of Ω^*. We then apply the algorithm described in Appendix A. Next, quadrilaterals in $\mathcal{T}^Q$ which intersect $\partial\Omega^*$ are identified and their projections onto Ω^* are collected in the set of boundary quadrilaterals $\mathcal{T}^Q_{\partial\Omega}$. Likewise, triangles in $\mathcal{T}^T$ whose projection onto Ω^* does not deteriorate are collected in $\mathcal{T}^T_{\partial\Omega}$. All other new quadrilaterals and all vertices outside of Ω^* which are not connected to quadrilaterals in $\mathcal{T}^Q_{\partial\Omega}$ are discarded.

Note that there are different approaches for the treatment of the boundaries. One possibility is the insertion of nodes (discs with vanishing radius) onto the boundaries. Another approach is the notion of quasi-discs as described e.g. in [BK01]. A quasi-disc results from an inclusion (close to the boundary) whose projection rays onto the boundary do not intersect any other inclusion. The projection on the boundary then is handled like an inclusion inside the domain.

Remark 4.1. Care has to be exercised to achieve a sufficiently high accuracy for the quadrature on the quadrilateral elements of $\mathcal{T}^Q$ since the transformation map can be highly nonlinear due to inclusions with very small distance. This is particularly critical for the evaluation of integrals of second derivatives as required for the residual error estimator. We employ an adaptive quadrature scheme which subdivides each $T \in \mathcal{T}^Q$ into $O(\log \delta^{-1})$ isotropic elements for which a conventional quadrature rule results in high accuracy. Here, δ is the distance of the two inclusions which are connected by T. Thus, the adapted quadrature does not adversely affect the quasi-optimal complexity of the method.

4.1. **Percolation.** In this experiment, we assume a set of equi-sized inclusions with increasing density. More specifically, the volume fraction $|\mathcal{B}_{\text{inc}}|/|\Omega^*|$ is increased successively up to a value where connected paths of (nearly) touching inclusions are formed. Along these, unhindered decrease of energy is possible and a sudden change of effective conductivity is to be expected. The percolation phenomenon becomes apparent from the energy graphs in Figure 5. In order to facilitate a dense packing, the distribution of inclusions is generated by starting with a structured distribution on a regular lattice and successive removal of random inclusions until the desired

density is reached. Depicted in Figure 5 are the energy and error graphs for inclusions with distances $\varepsilon = 10^{-2}, 10^{-4}, 10^{-6}, 10^{-8}$. Additionally, upper and lower energy bounds subject to the averaged a posteriori error estimator are plotted. The averages of 100 samples for each setting are plotted. It is expected that the maximal energy increases with smaller distances of inclusions. This is verified numerically in the graphs. The moderate decrease of the a posteriori error estimator can be attributed to the increased approximation quality with more inclusions since these are equivalent to degrees of freedom.

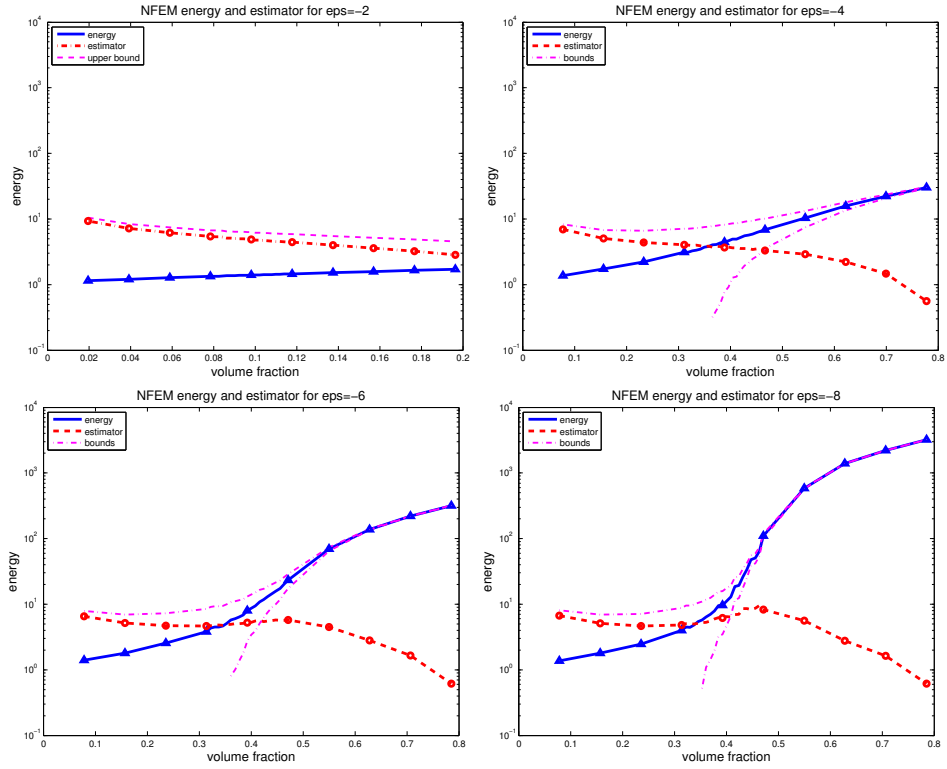

FIGURE 5. Average energy and a posteriori error estimator for a structured distribution of inclusions with distances $\varepsilon = 10^{-2}, 10^{-4}, 10^{-6}, 10^{-8}$. Upper and lower energy bounds due to the error estimator.

This standard setting can frequently be found in the literature. For instance, it is also examined in [KK10, BK01, Kol07].

4.2. **Model validation.** This subsection is concerned with the comparison of some structured and some random distribution of inclusions with equal volume fraction up to VF $= 0.5$ for all domains. Our experiments illustrate that a distribution based on a structured setting exhibits fundamentally

different behaviour than a random distribution. In particular, the percolation effect which is based on a very dense packing and the formation of some closed path through the domain as discussed in the last section cannot be observed with entirely randomly dispersed inclusions although the same amount of inclusions exists in the domain. In Figure 7, the energy graphs for the structured and the random case are depicted. We also plot the upper bound of the energy subject to the a posteriori error estimator, respectively.

This interesting finding questions the assumption of a structured distribution or periodicity in the limit which is the basis for homogenization and many multiscale approaches.

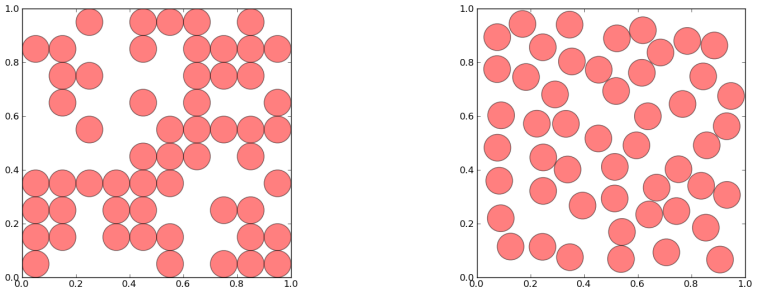

FIGURE 6. Structured and random test domains with equal volume fraction.

5. CONCLUSIONS AND OUTLOOK

This last section is devoted to some conclusions regarding the presented Network FEM. The method benefits from its relation to network methods as well as from its features inherited from classical FEM. From the former, the resolution of the small geometrical features of the domain with quasi-optimal complexity is derived. The latter enables the reliable and efficient error control for the discretisation error with an a posteriori error estimator. While being related to these two approximation methods, the Network FEM on the one hand is very flexible with regard to the size and shape of the inclusions and may be generalized to other settings. On the other hand, it does not suffer from the computational complexity induced by a possibly very fine mesh.

The proposed method may be understood as a discretisation model for the material behaviour of composite materials. The computational complexity is minimal since it is proportional to the complexity of the data complexity, i.e. the number of inclusions. At the same time, it sustains the critical structural material properties.

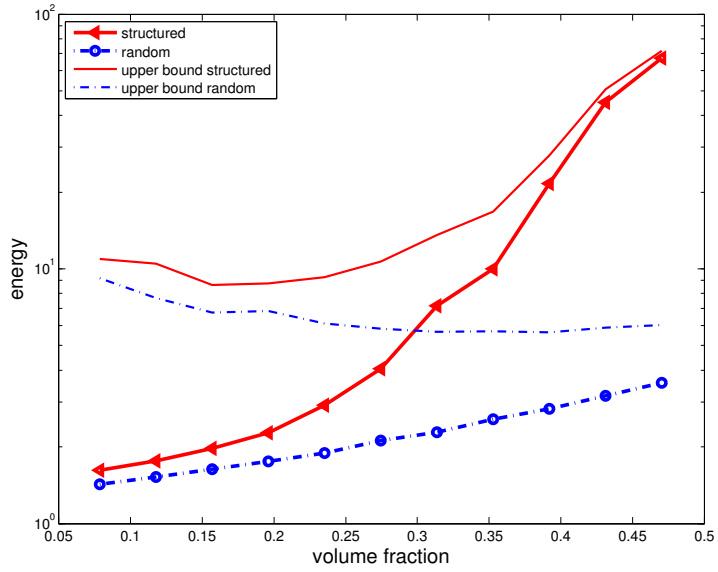

FIGURE 7. Energy for structured and random test domains with energy upper bound due to a posteriori error estimator.

In an upcoming paper, we will address the application of the method to more complex problems and discuss some aspects of the practical realization.

APPENDIX A.

In this appendix, we provide an algorithmic description for the generation of the generalized mesh of the Network FEM.

Voronoi diagram of the inclusions. Pivotal to the construction of an appropriate mesh for the complex geometry of the matrix $\Omega = \Omega_{\mathrm{mat}}$ is the (additively weighted) Voronoi diagram with regard to the set of discs $\mathcal{B}$. We refer to [AK00, Ede06] and references therein. We mark sets of the Voronoi construction by a subscript $\circ$. In case of equi-sized discs, the Voronoi cells $C \in \mathcal{C}_\circ$ are defined by straight line segments which become curved when the disc radii differ, see Figure 2. Each Voronoi cell $C \in \mathcal{C}_\circ$ is defined by a set of Voronoi edges $E \in \mathcal{E}_\circ$ and each edge is defined by two Voronoi vertices in the set of Voronoi vertices $\mathcal{N}_\circ(\Omega)$. For notational convenience,

we define the following maps which relate these entities.

for neighbours

$B_1, B_2 \in \mathcal{B}$: $\mathcal{E}_\circ(B_1, B_2)$ unique Voronoi edge associated with B_1, B_2, i.e.
$\mathcal{E}_\circ(B_1, B_2) := \{x \in \mathbb{R}^2 \mid \operatorname{dist}(x, B_1) = \operatorname{dist}(x, B_2) = \min_{B\in\mathcal{B}} \operatorname{dist}(x, B)\}$

$\forall B \in \mathcal{B}$: $\mathcal{E}_\circ(B)$ set of Voronoi edges associated to disc B, i.e.
$\mathcal{E}_\circ(B) := \{\mathcal{E}_\circ(B, B_1) \mid B_1 \in \mathcal{B} \text{ and } \mathcal{E}_\circ(B_1, B) \in \mathcal{E}_\circ\}$

$\forall E \in \mathcal{E}_\circ$: $\mathcal{N}_\circ(E)$ set of two vertices of edge E

$\forall E \in \mathcal{E}_\circ$: $\mathcal{B}(E)$ set of two neighboring discs, i.e., with $E = \mathcal{E}_\circ(B_1, B_2)$,
$\forall x \in E \operatorname{dist}(x, B_1) = \operatorname{dist}(x, B_2) = \min_{B\in\mathcal{B}} \operatorname{dist}(x, B)$

$\forall p \in \mathcal{N}_\circ$: $\mathcal{B}(p)$ set of neighboring discs, i.e.
$B(p) = \{B \in \mathcal{B} \mid \operatorname{dist} p, B = \min_{\tilde{B}\in\mathcal{B}} \operatorname{dist}(p, \tilde{B})\}$.

Our construction process for the mesh generates two types of elements. First, a parametric quadrilateral is obtained for each Voronoi edge $E \in \mathcal{E}_\circ$ which results in the set of quadrilaterals $\mathcal{T}^Q$. Second, the remaining polygonal areas $\Omega \setminus \bigcup \mathcal{T}^Q$ are decomposed into the set of triangles $\mathcal{T}^T$. The union then fulfils $\bigcup \mathcal{T}^T \cup \bigcup \mathcal{T}^Q = \Omega$ and we set $\mathcal{T} := \mathcal{T}^Q \cup \mathcal{T}^T$ the subdivision of Ω. The set of edges is denoted by $\mathcal{E}$, the restriction to interior edges is $\mathcal{E}_{\text{int}} := \{E \in \mathcal{E} \mid E \cap \Omega \neq \emptyset\}$ and the restriction to boundary edges on Γ is defined by $\mathcal{E}(\Gamma)$.

The notation and further details are provided in the following Subsections. A similar construction in the context of the network approximation method can be found in [BK01].

Local construction of quadrilaterals. For some Voronoi edge $E \in \mathcal{E}_\circ$ with Voronoi vertices $\{p_1, p_2\} = \mathcal{N}_\circ(E)$, the corresponding discs with centers $c_1, c_2 > 0$ are $\{B_1, B_2\} = \mathcal{B}(E)$. We connect center c_1 with p_1 and p_2 and denote the intersections with disc B_1 by a_1 and b_1, respectively. The same is done with c_2 which results in a_2, b_2. The parametric quadrilateral element $Q_E \in \mathcal{T}^Q$ of edge E is then defined by the line segments $\overline{a_1a_2} = \operatorname{conv}\{a_1, a_2\}$, $\overline{b_1b_2} = \operatorname{conv}\{b_1, b_2\}$ and the sections on the discs B_1, B_2 which lie in between a_1, b_1 and a_2, b_2, respectively.

This procedure has to be carried out for all edges $E \in \mathcal{E}_\circ$ and provides the set of curvilinear quadrilaterals $\mathcal{T}^Q$. Note that if either one or both of the discs deteriorate to a point, we obtain either a curvilinear triangle or a line segment. The latter case is discarded.

Remark A.1. Note that the Voronoi dual edge might not be connected (see Figure 8). The same applies to the corresponding parametric quadrilaterals

Algorithm 1 geometry adapted mesh construction

Require: domain Ω^*, set of discs $\mathcal{B}$
  return triangulation $\mathcal{T} = \mathcal{T}^Q \cup \mathcal{T}^T$ of $\Omega = \Omega^* \setminus \mathcal{B}$ into parametric quadrilaterals $\mathcal{T}^Q$ and triangles $\mathcal{T}^T$
  $(\mathcal{C}_\circ, \mathcal{E}_\circ, \mathcal{N}_\circ) \leftarrow$ compute Voronoi diagram for $(\Omega, \mathcal{B})$
  $\mathcal{T}^Q \leftarrow \emptyset, \quad \mathcal{T}^T \leftarrow \emptyset$ {initialization}
  for all $E \in \mathcal{E}_\circ$ **do**
    $(B_1, B_2) \leftarrow \mathcal{B}(E)$ neighbor discs associated with E
    $a, b \leftarrow$ vertices of E
    $c_1, c_2 \leftarrow$ centers of B_1, B_2
    $a_1, b_1 \leftarrow$ intersection of line segments $\overline{c_1 a}$ and $\overline{c_1 b}$ with ∂B_1
    $a_2, b_2 \leftarrow$ intersection of line segments $\overline{c_2 a}$ and $\overline{c_2 b}$ with ∂B_2
    $s_1 \leftarrow$ boundary segment of ∂B_1 between a_1 and b_1
    $s_2 \leftarrow$ boundary segment of ∂B_2 between a_2 and b_2
    $\mathcal{T}^Q \leftarrow \mathcal{T}^Q \cup$ parametric quadrilateral $(s_1, \overline{a_1 a_2}, s_2, \overline{b_2 a_2})$
  end for
  for all $P \in \mathcal{N}_\circ$ **do**
    $\Lambda \leftarrow \mathcal{B}(P)$ discs associated with Voronoi vertex P
    $c_1, \dots, c_n \leftarrow$ centers of discs $B \in \Lambda$
    $A \leftarrow \emptyset$ {initialization}
    for all $B \in \Lambda$ **do**
      $c \leftarrow$ center of B
      $A \leftarrow A \cup \{a\}$ intersection of line segment $\overline{cP}$ with ∂B
    end for
    $\mathcal{T}^T \leftarrow \mathcal{T}^T \cup$ decomposition of conv(A) into triangles
  end for
  $\mathcal{T} \leftarrow \mathcal{T}^Q \cup \mathcal{T}^T$

as can be seen in the same figure. We denote the number of connected components of $T \in \mathcal{T}^Q$ by $K(T)$. The parametrisation from Definition 2.1 applies to every connected component of T.

Triangles. The above algorithm yields the set $\mathcal{T}^Q$ and the entire surface of each disc is associated with a set of quadrilaterals from the set $\mathcal{T}^Q$, i.e., for any $B \in \mathcal{B}$, $\partial B = \bigcup_{Q \in \mathcal{T}^Q(B)} B \cap Q$. The remaining areas in Ω^* which are not occupied by either a disc or a quadrilateral are polygons. In fact, a polygon P_p with n edges is associated with each Voronoi vertex $p \in \mathcal{N}_\circ$ where $n = \#\mathcal{B}(p)$ and $P_p := \text{conv}\{a_1, \dots, a_n\}$ with $a_1, \dots, a_n$ the intersection points of the connections of the disc centers of each $\mathcal{B}(p)$ with p. We decompose each such polygon into a set of triangles which results in the set $\mathcal{T}^T$. The adapted triangulation is then given by $\mathcal{T} := \mathcal{T}^Q \cup \mathcal{T}^T$.

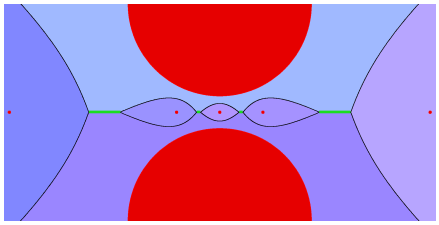

(a) Detail of a generalized Voronoi diagram with a multiply connected Voronoi edge.

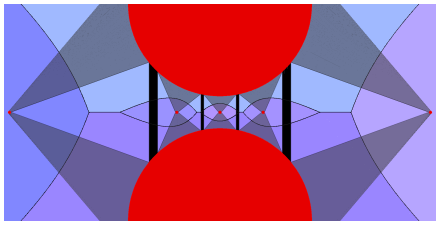

(b) Detail of the corresponding finite element grid with multiply connected parametric quadrilateral (black shaded) T ($K(T) = 4$).

FIGURE 8. Generalized Voronoi and corresponding grid; Voronoi edges and corresponding parametric quadrilateral multiply connected.

REFERENCES

[ABP78] J.-L. Lions A. Bensoussan and G. Papanicolaou. *Asymptotic Analysis for Periodic Structures*. North-Holland Publ., 1978.

[AK00] Franz Aurenhammer and Rolf Klein. Voronoi diagrams. In *Handbook of computational geometry*, pages 201–290. North-Holland, Amsterdam, 2000.

[AO00] M. Ainsworth and J.T. Oden. *A posteriori error estimation in finite element analysis*. Wiley-Interscience [John Wiley & Sons], New York', 2000.

[BK01] Leonid Berlyand and Alexander Kolpakov. Network approximation in the limit of small interparticle distance of the effective properties of a high-contrast random dispersed composite. *Arch. Ration. Mech. Anal.*, 159(3):179–227, 2001.

[BN02] Leonid Berlyand and Alexei Novikov. Error of the network approximation for densely packed composites with irregular geometry. *SIAM J. Math. Anal.*, 34(2):385–408 (electronic), 2002.

[BP89] N.S. Bakhvalov and G.P. Panasenko. *Homogenization: Averaging Processes in Periodic Media*. Kluwer Academic Publ., 1989.

[BP98] Liliana Borcea and George C. Papanicolaou. Network approximation for transport properties of high contrast materials. *SIAM J. Appl. Math.*, 58(2):501–539 (electronic), 1998.

[CD00] D. Cioranescu and P. Donato. *An Introduction to Homogenization*. Oxford University Press, 2000.

[CF00] C. Carstensen and S. A. Funken. Constants in Clément-interpolation error and residual based a posteriori error estimates in finite element methods. *East-West J. Numer. Math.*, 8(3):153–175, 2000.

[CP12] C. Carstensen and D. Peterseim. Finite element network approximation of conductivity in particle composites. *Numer. Math.*, (accepted) 2012.

[Ede06] Herbert Edelsbrunner. *Geometry and topology for mesh generation*, volume 7 of *Cambridge Monographs on Applied and Computational Mathematics*. Cambridge University Press, Cambridge, 2006. Reprint of the 2001 original.

[Gri92] G. Grimet. *Percolation*. Springer-Verlag, 1992.

[JKO94] V.V. Jikov, S.M. Kozlov, and O.A. Oleinik. *Homogenization of Differential Operators and Integral Functionals*. Springer-Verlag, 1994.

[Kel63] J.B. Keller. Conductivity of a medium containing a dense array of perfectly conducting spheres or cylinders or nonconducting cylinders. *J. Appl. Phys.*, 34(4):991993, 1963.

[Kes92] H. Kesten. *Percolation Theory for Mathematicians*. Birkhäuser, 1992.

[KK10] A. A. Kolpakov and A. G. Kolpakov. *Capacity and transport in contrast composite structures*. CRC Press, Boca Raton, FL, 2010. Asymptotic analysis and applications.

[Kol07] A. Kolpakov. Numerical verification of the existence of the energy-concentration effect in a high-contrast heavy-charged composite material. *Journal of Engineering Physics and Thermophysics*, 80:812–819, 2007. 10.1007/s10891-007-0109-6.

[KS64] H. Keller and D. Sachs. Calculations of the conductivity of a medium containing cylindrical inclusions. *J. Appl. Phys.*, 35:537538, 1964.

[MNS09] Shipeng Mao, Serge Nicaise, and Zhong-Ci Shi. On the interpolation error estimates for Q_1 quadrilateral finite elements. *SIAM J. Numer. Anal.*, 47(1):467–486, 2008/09.

[Pet12] D. Peterseim. Robustness of finite element simulations in densely packed random particle composites. *Networks and Heterogenous Media*, 7(1):113–126, 2012.

[Ste70] Elias M. Stein. *Singular integrals and differentiability properties of functions*. Princeton Mathematical Series, No. 30. Princeton University Press, Princeton, N.J., 1970.

[Ver96] R. Verfürth. *A review of a posteriori error estimation and adaptive mesh-refinement techniques*. Wiley-Teubner, 1996.

(M. Eigel, D. Peterseim) Humboldt-Universität zu Berlin, Unter den Linden 6, 10099 Berlin, Germany.

E-mail address: eigel@mathematik.hu-berlin.de, peterseim@mathematik.hu-berlin.de